Microstructure, texture evolution, mechanical properties and corrosion behavior of ECAP processed ZK60 magnesium alloy for biodegradable applications

Ehsan Mostaed[a,*], Mazdak Hashempour[b], Alberto Fabrizi[c], David Dellasega[d], Massimiliano Bestetti[b], Franco Bonollo[c], Maurizio Vedani[a]

a
 Department of Mechanical Engineering, Politecnico di Milano, Milan, Italy
b
 Department of Chemistry, Materials and Chemical Engineering "Giulio Natta", Politecnico di Milano, Via Mancinelli 7, 20131 Milano, Italy
cDepartment of Management and Engineering, Università di Padova, Stradella S. Nicola 3, 36100 Vicenza, Italy
dDepartment of Energy, Politecnico di Milano, 20156 Milan, Italy.

*Corresponding author.

1. Introduction

Magnesium and its alloys have been receiving much interest as promising material candidates in the field of biodegradable devices such as stents and several orthopedic applications in recent years. That is, due to its excellent properties such as low density and high specific strength, relatively low corrosion resistance and elastic modulus closer to that of bones when compared to other implant metallic materials, Mg has been considered as a more versatile material in bio applications (Gu and Zheng, 2010; Saris et al., 2000; Witte et al., 2008; Zeng et al., 2008). Moreover, magnesium is one of the abundant nutritionally essential elements in the human body. Song (2007) showed that magnesium alloys could be dissolved in the human body without causing any detrimental effects. However, its intense degradation rate leads to a premature loss of mechanical integrity before satisfying its intended function in the human body. To be effectively used as biodegradable materials, Mg alloys are required to possess appropriate mechanical properties all over their service life and they should be composed of bio-safe alloying elements to assure the biocompatibility, non-toxicity, cytocompatibility. Hence, mechanical and corrosion improvement of Mg and of selected Mg alloys are of paramount importance for this field (Gunde et al., 2011; Hermawan et al., 2010).

Several studies have already been published on methods to enhance mechanical and corrosion properties by adding the most popular and effective alloying elements. However, investigations on Mg alloys containing Al and rare-earth elements demonstrated that these alloys are potentially toxic since Al is a risk factor for Alzheimer's disease and also some rare-earth elements such as Yttrium may cause liver toxicity (Saris et al., 2000; Wang et al., 2006). Witte et al. (2008) stated that for the use in humans, aluminium-free magnesium alloy systems are recommended. As an alloying element, Zn could be conveniently considered for this application. Small amounts of Zn into Mg can improve the ductility and deformability. In addition, Zn is one of the essential nutritive elements for the human body and it is known that released Zn ions can be easily absorbed without harming vital organs. Zirconium, in small content, has also been considered as a biocompatible element (Emley, 1966; Gu and Zheng, 2010). In addition, Gu et al. demonstrated that additions of Zn and Zr to Mg lead to strength improvement as well as reduction of corrosion rate and good cytocompatibility, compared to pure Mg (Goodman et al., 1993; Gu et al., 2009).

Previous studies proved that grain refinement of magnesium alloys is one of the most efficient ways to improve mechanical properties as well as for promoting more uniform corrosion behavior due to the homogeneous distribution of the nano-sized second phases. These properties can be achieved especially when severe plastic deformation techniques are exploited to produce ultra-fine grained (UFG) materials with sub-micrometer grain size (Alvarez-Lopez et al., 2010; Gao et al., 2011; Ge et al., 2013; Mostaed et al., 2013; Yamashita et al., 2001). Moreover, Argade et al. (2012) reported that UFG Mg–Y–RE alloy possess an improved polarization resistance and the most positive pitting potentials with respect to coarse-grained reference alloy.

From mechanical point of view, as hexagonal close-packed metal magnesium has a limited ductility and poor formability at room temperature due to an inadequate number of active deformation systems. Furthermore, formation of strong crystallographic texture upon plastic deformation processing brings about a strong tension—compression strength anisotropy attributed to $\{1\,0\,\bar{1}\,2\}\langle 1\,0\,\bar{1}\,1\rangle$ twinning system which is easily activated by a compressive stress applied parallel to the basal planes or by a tensile stress applied perpendicular to the basal plane (Bohlen et al., 2007; Pérez-Prado and Ruano, 2002; Wang and Huang, 2007).

In this paper, a UFG commercial Mg–Zn–Zr alloy was processed by severe plastic deformation to achieve a UFG structure in order to improve strength as well as to induce mechanical isotropic behavior by attenuating the crystallographic texture. A three-step procedure of equal channel angular pressing (ECAP) was exploited with decreasing processing temperature levels to improve grain size refinement and processing efficiency. Microstructural evolution, mechanical properties in tension and compression and corrosion properties of ZK60 Mg alloy processed via ECAP are presented to improve the knowledge about possible processing routes for biodegradable alloys

2. Experimental procedure

2.1. Materials and ECAP processing

In this research, ECAP was performed on a commercial ZK60 (Mg–5.3Zn–0.48Zr, wt%) wrought alloy. The starting extruded
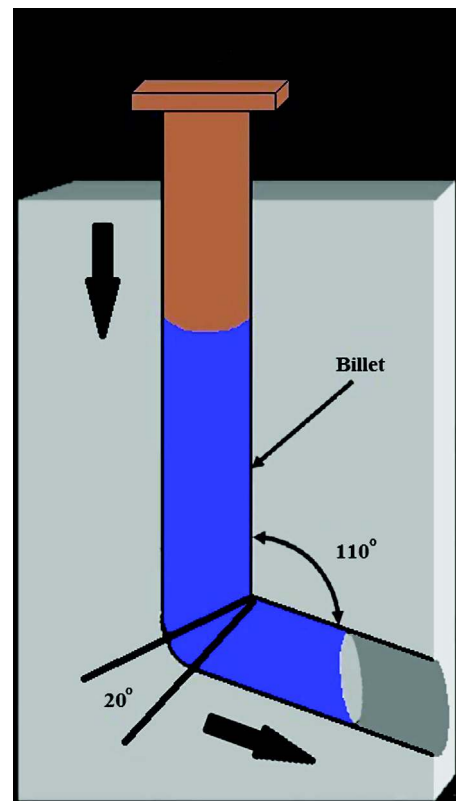

Fig. 1 – Schematic illustration of ECAP process.

Samples	ECAP temperature (°C)	Number of ECAP passes
A	NA	NA
E1	250	4
E2	200	4
E3	150	4
E4	150	6
E5	150	8

bars were machined into billets with a diameter of 10 mm and a length of 100 mm. As it is illustrated in Fig. 1, the adopted ECAP die had two cylindrical channels intersecting at an angle of 110° and with an outer arc of curvature of 20°, supplying an equivalent strain of ~0.76 on each pass (Iwahashi et al., 1996). The die was homogeneously heated by 4 electrical resistance heaters placed along the vertical channel and at the intersection point of the channels and the temperature was monitored throughout the process using a thermocouple inserted in the die. All multiple pressings were executed by rotating in the same direction the sample along their longitudinal axis by 90° before each new pass (route B_c according to established designation given in the literature (Segal, 1999). The billets were pressed into the ECAP die with a speed of 30 mm/min using molybdenum disulfide (MoS_2) as lubricant. It has been demonstrated in an earlier work (Ge et al., 2013) that processing of starting coarse grained Mg alloy billets below a threshold leads to extensive cracking due to lack of adequate ductility. Increasing the processing temperature significantly improved the formability and allowed obtaining defect free billets. Accordingly, in this study the strategy of performing a first set of passes at relatively high temperature (250 °C) to achieve a primary significant grain-size reduction and then completing the refinement to UFG scale through two subsequent temperature steps namely, 200 °C and 150 °C. Table 1 summarizes the ECAP conditions for the different temperature and number of applied passes hereafter referred to.

2.2. Microstructural observation

The materials used for microstructural characterization included the as received alloy and ECAP processed billets. Samples were cut along their longitudinal cross-section, polished and etched in a solution of 6 g picric acid, 5 ml acetic acid, 10 ml water and 100 ml ethanol. Field-emission gun scanning electron microscopy (FEG-SEM) was used to observe the microstructure of samples.

2.3. Texture characterization

Microstructural evolution of the ZK60 alloy processed by ECAP was investigated by Electron Backscattered Diffraction (EBSD) technique. In particular, distribution of grain size, crystallographic texture and grain orientation maps of the ZK60 alloy in the as-received condition and after ECAP process were obtained using EBSD technique interfaced with

a (FEG-SEM). The EBSD analyses were performed on the A, E2, E3 and E5 samples and the resulting EBSD maps were taken from the billet's longitudinal section that is, the plane parallel to the processing direction (flow plane). All the data were then processed with TSL OIM™ software. The typical scan area was 30 μm × 30 μm with a 0.2 μm step size for the ECAP-processed specimens, while, in order to achieve good statistical data due to the presence of coarser grains, a larger scan area was selected for as-received alloy samples. Prior to EBSD analysis, all specimens' surfaces were carefully prepared by standard mechanical polishing followed by low-angle ion milling.

2.4. Mechanical characterization

Mechanical properties were assessed by tensile, compression, and Vickers micro-hardness tests. Tensile specimens with a gauge length of 12 mm and the diameter of 4 mm were machined along the longitudinal direction of the specimens and tested at room temperature at an initial strain rate of $10^{-3}\,s^{-1}$. For compression tests, cylindrical specimens with diameter of 10 mm and height of 20 mm were cut from the as-received and ECAP billets. In each condition 3 samples for tensile and compression tests were prepared and tested. Measurements of micro-hardness were made on the plane parallel and perpendicular to the extrusion and ECAP direction with an indenter load of 1 N.

2.5. Electrochemical measurements

The corrosion behavior of as-received and ECAP processed ZK60 samples was studied by performing open circuit potential (OCP) and potentiodynamic polarization tests, adopting a standard three-electrode cell set-up, in a phosphate buffer solution (PBS), at 37 °C. This solution is an isotonic saline electrolyte buffered at pH 7.4 in order to simulate the body fluids.

Samples were cut from either as received or ECAP treated billets, in the form of cylindrical discs of 9 mm diameter and 3 mm thickness. A PTFE sample holder with a circular opening of 5.5 mm diameter was used to expose an area of 23.8 mm² of the samples to the electrolyte.

A silver chloride electrode (Ag/AgCl, sat. KCl, +197 mV vs. SHE) and a platinum coated titanium sheet were used as the reference and counter electrodes, respectively. Electrochemical tests were conducted using a Model 7050 AMEL—Potentiostat/Galvanostat. After measuring the OCP for 18 h, the potential window for potentiodynamic polarization was selected from −250 mV vs. OCP to +900 mV vs. OCP. Then, for standardizing the procedure, the potential window of −1.9 V to −0.8 V vs. Ag/AgCl and a scan rate of 0.166 mV/s was considered for all of the samples. Extrapolation of the polarization curves was performed according to ASTM standard (ASTM-G102-89, 1989) and used to estimate the corrosion rates of the samples.

2.6. Weight loss measurement

The immersion tests were performed in PBS solution for 96 h. The corrosion products were removed from the samples by dissolution in chromic acid solution (200 g/l Cr_2O_3+10 g/l $AgNO_3$).

Immediately after acid cleaning, samples were washed with ethanol and then dried. Weight loss was measured (balance sensitivity 0.0001 g) and corrosion rate per unit surface area and time was calculated.

3. Results and discussion

3.1. Microstructure

Fig. 2 shows EBSD map and SEM image of the as-received ZK60 alloy (sample A) taken on the longitudinal cross-section. The starting alloy featured a rather heterogeneous and incompletely recrystallized microstructure with a bimodal grain size distribution of coarse grains of about 10–20 μm coexisting with a large number of dynamically recrystallized (DRXed) grains with a size of about 1–2 μm clustered near the band of secondary phase particles (black dots). Furthermore, as it is highlighted by two ellipses in Fig. 2a, most of the secondary-phase particles were distributed along the extrusion direction, which is attributed to the phenomenon of particle stimulated nucleation (PSN) (Robson et al., 2009), leading to formation of high-stress zones around these hard phases which accelerate the DRX process and promoting the grain refinement effect. It should also be mentioned that the pinning effect of the fine secondary phases inhibited the growth of DRXed grains in the aforementioned zones.

In addition, the segregation bands clearly highlighting the deformation flow-lines parallel to the extrusion direction could be better perceived from SEM images taken in back-scattered electron (BSE) mode (Fig. 2b). Energy-dispersive spectroscopy (EDS) analysis presented in Table 2 indicates the elemental composition of the four representative points marked with letters A–D on the SEM image of Fig. 2b. Point A is representative of the α-Mg solid solution matrix with little amount of Zn. EDS results shows that point B represents one of those above mentioned segregation bands of mainly enriched of Mg–Zn–Zr compounds. Moreover, point C and D display two types of precipitates, a first phase very rich in Zr and Zn, together with small Mg–Zn compound, respectively.

Fig. 3 depicts the EBSD map evolution of ZK60 alloy samples and the corresponding distribution of grain size during ECAP processing. The microstructure of sample E2 shown in Fig. 3a (4 passes at 250 °C plus additional 4 passes at 200 °C) shows a remarkable grain refinement. However, some coarse grains representing the residual part of the original structure are still visible. Eventually, after 4 more passes at 150 °C those residual grains became refined, resulting in the achievement of an uniform and completely recrystallized microstructure formed by ultra-fine grains of 0.6 μm average size, as shown in Fig. 3b. Therefore, it can be stated that ECAP promotes a significant grain refinement in Mg alloy through the DRX mechanism. It is noteworthy that such a remarkable grain refinement can also be attributed to the an initial fine grain structure of ZK60 alloy since the initial grain size distribution of the magnesium alloys plays a critical role both in controlling the rate and development of grain refinement and in determining the final grain structure after ECAP. That is, an initial fine grain structure can facilitate the grain refinement process in Mg alloys due to the high density of
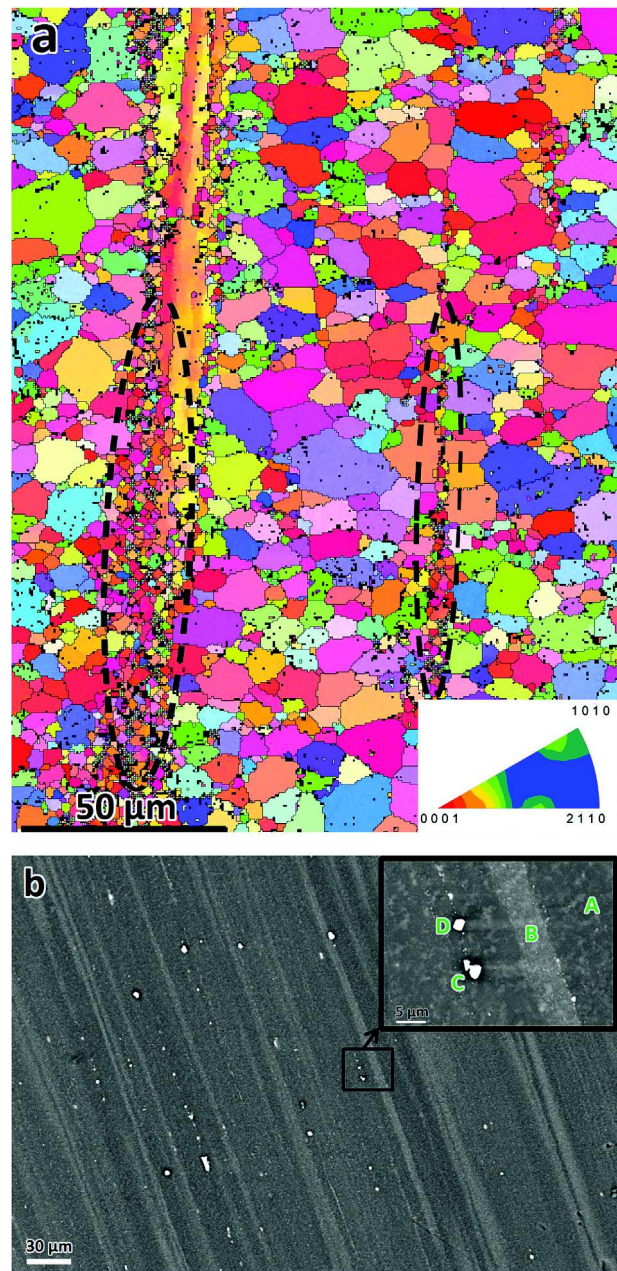

Fig. 2 – Typical microstructure of sample A. (a) EBSD map and (b) SEM micrograph showing representative points A–D referring to the EDS analysis (Table 2).

Table 2 – EDS analysis of the sample A. Letters A–D refer to the representative regions shown in Fig. 1.			
Position	Mg (wt%)	Zn (wt%)	Zr (wt%)
A	98.5	1.5	–
B	88.0	8.7	3.4
C	13.7	27.9	58.4
D	49.2	50.8	–

grain boundaries. Fig. 4 shows a high magnification micrograph of E3 sample, in which distinct second-phase particles are highlighted. The elemental compositions of second
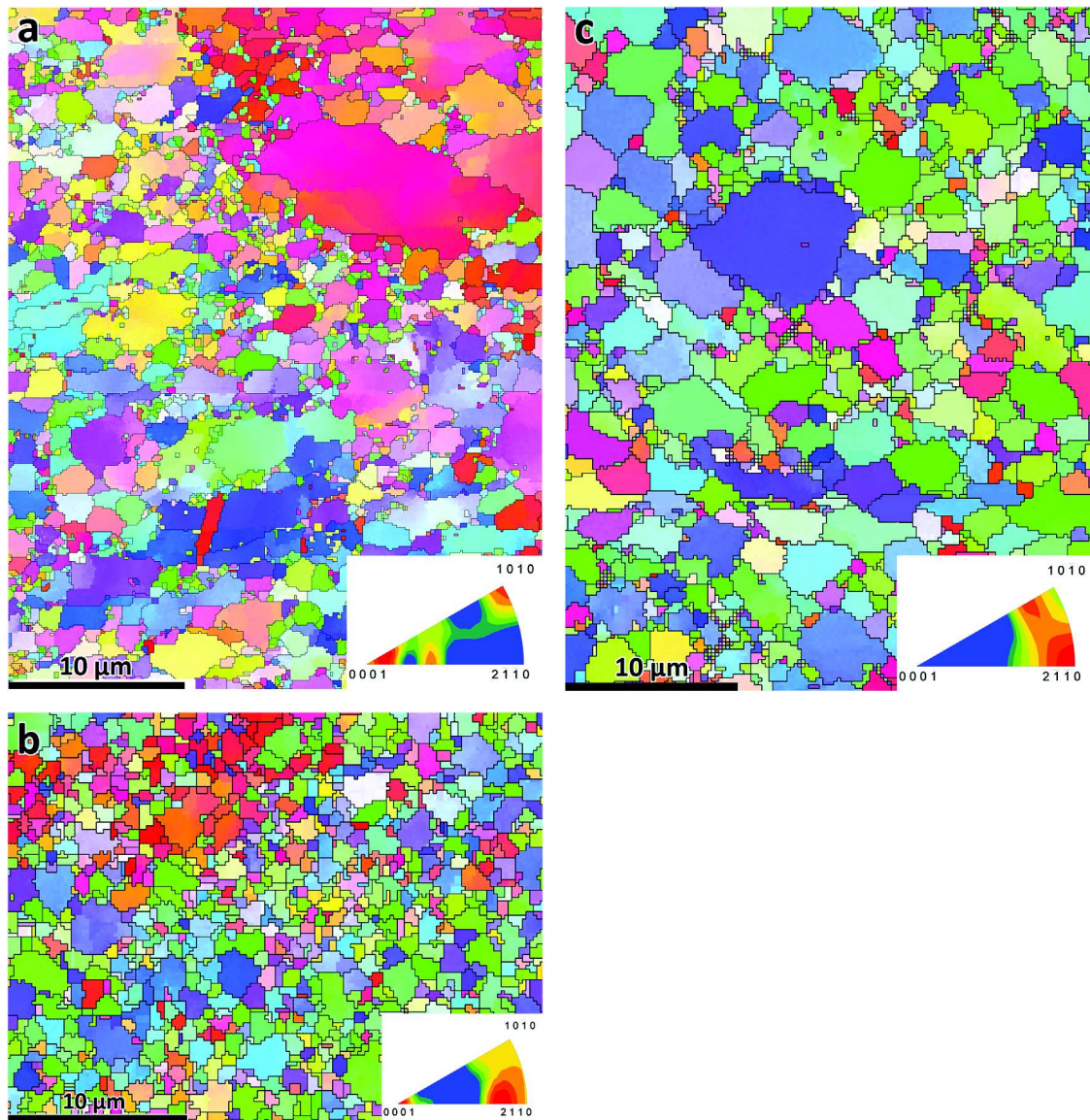
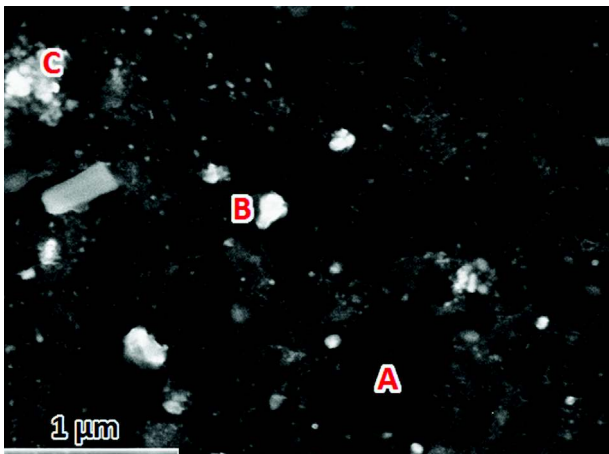Fig. 3 – EBSD inverse pole figure of ZK60 after ECAP: sample E2 (a), E3 (b) and E5 (c).

Fig. 4 – High magnification image of sample E3. Representative phases for EDS analyses A, B, C are highlighted.

Table 3 – EDS analysis of phases A, B, C highlighted in Fig. 3.

Point	Mg (wt%)	Zn (wt%)	Zr (wt%)
A	96.4	3.6	–
B	89.4	10.6	–
C	74.0	20.8	5.2

phases are listed in Table 3. Accordingly, careful observation of Fig. 4 reveals that through ECAP, not only did the solid solubility of Zn in α-Mg matrix increased, but also Mg–Zn and Mg–Zn–Zr compounds are broken into much smaller particles and finely dispersed in the alloy matrix.

As shown in Fig. 3c, additional 4 ECAP passes at the same temperature (150 °C) resulted in grain growth that was

detected in sample E5, with a resulting average grain size of about 1 μm. It is noteworthy that grain coarsening in this UFG Mg alloy might be due to recrystallization and a rapid grain growth caused by relatively high processing temperature and the interpass time spent at processing temperature. This increase in the average grain size was also observed in other research works (Dumitru et al., 2014; He et al., 2010). Furthermore, the activation energy for grain growth of the fine-grained Mg alloy is markedly lower than that of the coarse-grained alloys (Miao et al., 2010). Hence, the authors suggest that the aforementioned difference in the activation energy is even more pronounced in the case of UFG Mg alloys since the grain boundaries of the UFG materials are in a non-equilibrium state and such boundaries are more likely to change to the equilibrium state. In addition, activation of non-basal slipping systems at the UFG scale caused by grain boundary compatibility stress (Koike et al., 2003) as well as grain boundary sliding (GBS) (Lu et al., 2014; Tan and Tan, 2003), results in a lower amount of energy required for deformation during ECAP process. Accordingly, it is supposed that this surplus energy made available might be consumed as a grain growth driving force.

3.2. Texture evolution

The {0 0 0 2} pole figures of as-extruded and ECAP processed ZK60 alloy are shown in Fig. 5. Sample A exhibits a typical extrusion (fiber) texture, with (0 0 0 2) planes oriented parallel to extrusion direction (ED). As ECAP processing progresses up to E2 sample, the dominant texture with basal planes parallel to ED becomes weaker although the stronger component with basal planes parallel to the ED almost remains. Accordingly, the typical texture of E2 sample is somewhat similar to the initial fiber texture. However, the maximum texture intensity increased from 5.7 to 9.2 as sample A underwent two steps of ECAP processing (E2). Subsequent step of ECAP, E3 sample, fully replaced the original fiber texture by a new stronger texture component with basal planes preferentially inclined by about 52° to the processing direction (Fig. 5c) and the maximum texture intensity increased up to 19.1. Finally, after 4 more passes at 150 °C (E5) the basal planes further rotated forming a dominant texture locating at 43° from ED. The maximum texture intensity of {0 0 0 2} pole figure for E5 then decreased to 15.8. Such orientations at which basal planes coinciding with ECAP shear plane are in good agreement with other previous findings reported for AZ alloys (Agnew et al., 2004; Del Valle
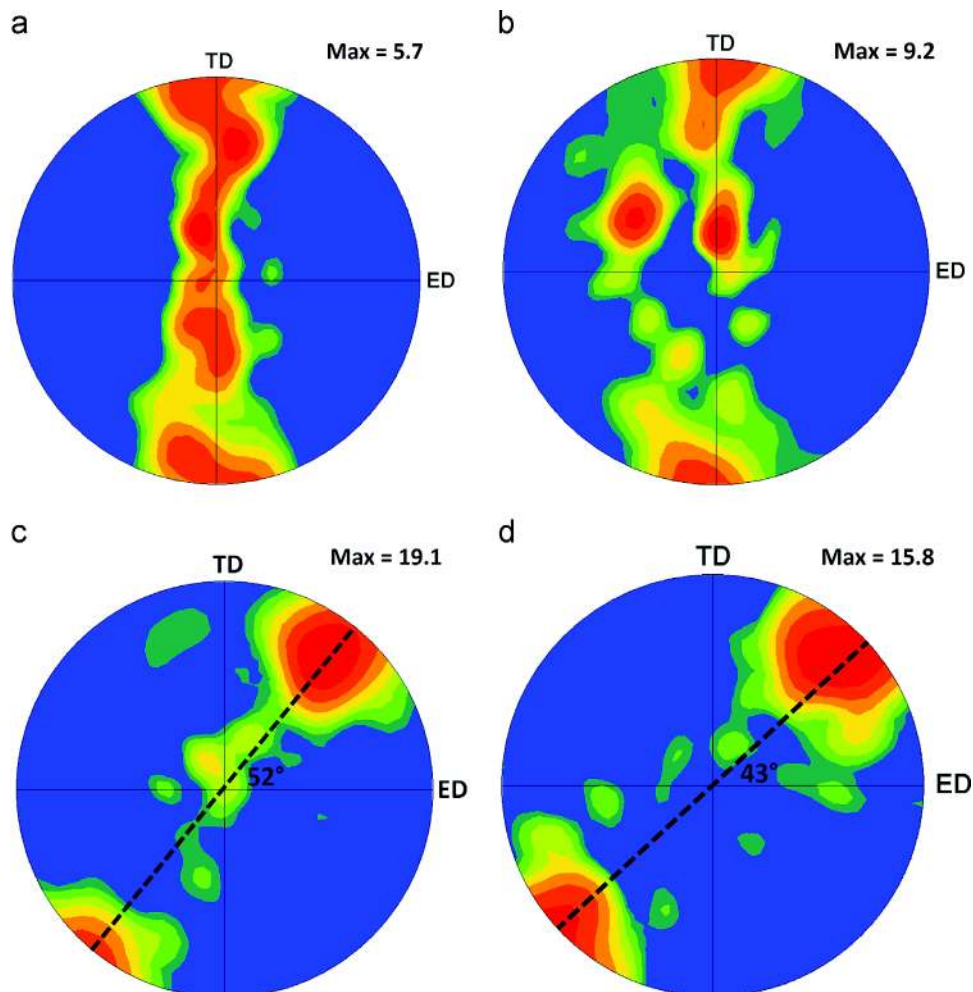

Fig. 5 – (0 0 0 2) pole figure showing the crystallographic texture of sample A (a), E2 (b), E3 (c) and E5 (d).
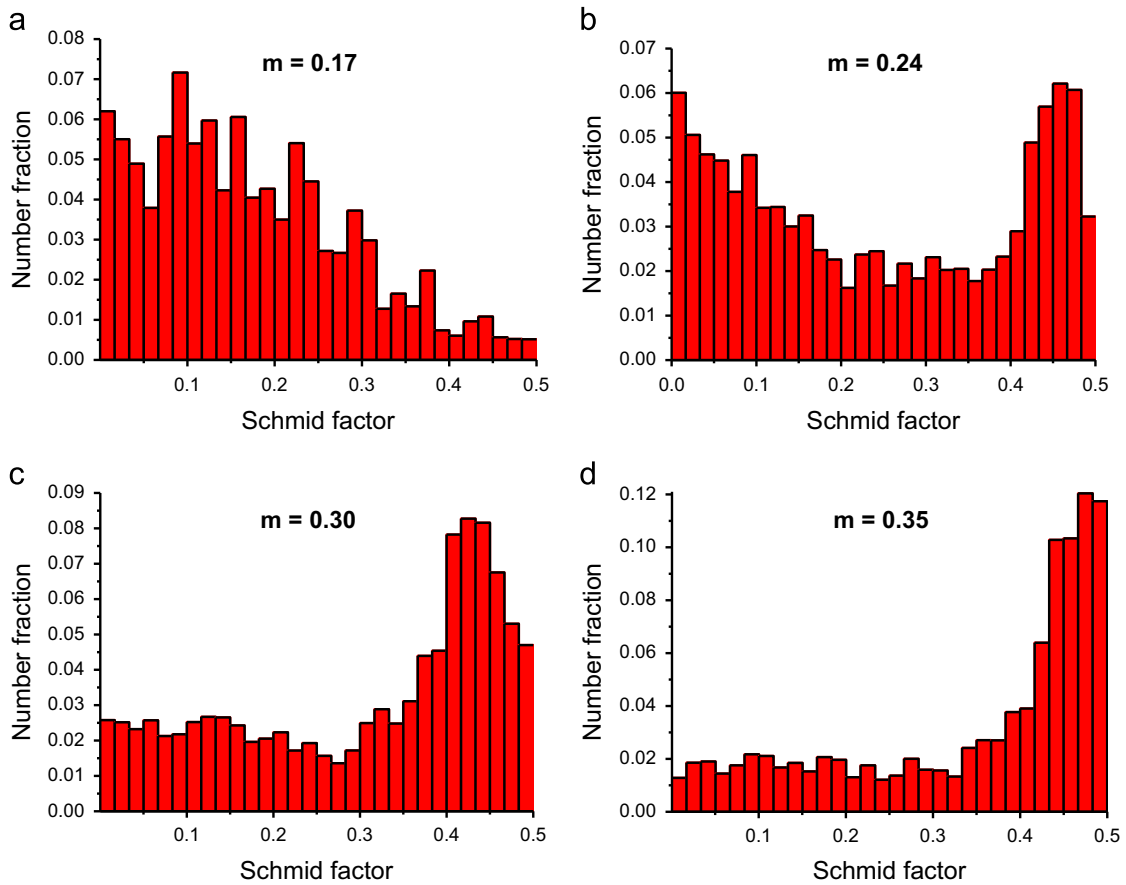
Fig. 6 – Distribution of Schmid factors for basal slip in the A (a), E2 (b), E3 (c), And E5 (d) samples.

et al., 2006; Kim et al., 2003, 2002). In brief, it should be noted that the extrusion fiber texture, whereby higher tensile strength along ED is achieved, is progressively destroyed and finally substituted by a new dominant texture developed at E3 condition and entirely stabilized after 4 subsequent passes (E5). Such a strong texture obtained by ECAP can be ascribed to the use of route B_c representing a highly redundant strain path (Gholinia et al., 2000).

Fig. 6 shows the distribution of Schmid factor for (0 0 0 1) $\langle 1\,1\,\bar{2}\,0\rangle$ basal slip in the as-extruded and ECAP processed samples. It can be observed that, with accumulation of ECAP passes, the value of Schmid factor gradually increases, leading to a significant improvement from 0.17 (A) to 0.30 and 0.35 for E3 and E5 samples, respectively. It is well known that in pure Mg at room temperature, the critical resolved shear stress (CRSS) of the basal slip system is 100 times lower than that of non-basal slip systems. That is, at room and moderately elevated temperatures plastic deformation is mostly governed by the basal slip system since other slip systems can hardly be activated (Hutchinson and Barnett, 2010; Máthis et al., 2004; Obara et al., 1973). Thus, the maximum Schmid factor for (0 0 0 1) $\langle 1\,1\,\bar{2}\,0\rangle$ slip can be achieved when basal planes are oriented with an angle of 45° to the stress axis. It is worth mentioning that for Mg and its alloys the orientation between basal plane and the applied stress axis is of major importance from a mechanical viewpoint, especially in terms of tensile strength and fracture elongation (Agnew

et al., 2004; Tang et al., 2009). Accordingly, the improvement in Schmid factor value by ECAP progress is in good agreement with evolution of basal plane orientation to the tensile axis, bringing higher values of 0.30 and 0.35 for E3 and E5 conditions, respectively. In short, Schmid factors for basal slip in E3 and E5 conditions are near maximum, giving rise to easy dislocation glide on the dominant slip plane (0 0 0 2) and thereby lowering the stress required for yielding.

3.3. Mechanical properties

3.3.1. Microhardness

Fig. 7 shows the Vickers micro-hardness variations of the ZK60 alloy measured on both longitudinal (LS) and transversal (TS) sections of the as-received and ECAP processed samples. For sample A, the hardness value on longitudinal section (67.5 HV) was higher than that measured on the transversal plane (63.7 HV), which is attributed to an intense texture inherited from extrusion, with the majority of the basal planes lying parallel to the extrusion direction, causing the generation of $\{1\,0\,\bar{1}\,2\}\,\langle 1\,0\,\bar{1}\,1\rangle$ twins (Chino et al., 2008). From the general trend it is clearly seen that, by increasing the number of ECAP passes and decreasing the processing temperature, the hardness of the alloy raises. Furthermore, the gap in hardness values between LS and TS was progressively reduced, implying that E3 sample behaves more homogenously. By further ECAP processing at 150 °C up to 8 passes
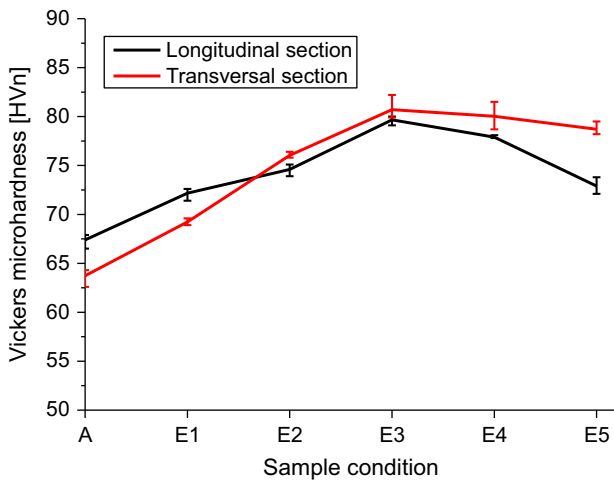
Fig. 7 – Hardness evolution as a function of sample condition.

(sample E5), the hardness was reduced on both sections (a drop of about 2% for TS samples, against nearly 9% for LS samples). Grain growth, texture modification as well as increasing Schmid factor from E3 to E5 samples, which were discussed in the previous section, are the main reasons responsible for the above-mentioned drop.

3.3.2. Tensile and compressive properties

The tensile and compressive stress versus strain curves for as extruded and for ECAP processed samples are depicted in Fig. 8. The 0.2% proof stress in tension (TYS) and compression (CYS), ultimate tensile strength (UTS) and tensile fracture elongation (TE) drawn from these curves are also plotted in Fig. 9. Considering that the grain structure was substantially refined with increasing number of ECAP passes and due to decreasing temperature, a progressive rise in strength would be expected both in compression and tension. Therefore, factors other than grain size should be considered in the present case to account for the observed trend. It is well known that Mg alloys, possessing hexagonal close packed (hcp) crystal lattice, form a marked texture with $(0\,0\,0\,1)$ crystal planes parallel to the extrusion direction. Since after extrusion the basal planes would be parallel to the tensile direction, the likelihood of activation of $\{1\,0\,\overline{1}\,2\}\,\langle 1\,0\,\overline{1}\,1\rangle$ twining system would lower in the tensile direction, then in the compression. Thus, the TYS is significantly higher than the CYS in the as extruded condition. The strong basal plane fiber extrusion texture (Fig. 5a) was gradually undermined by ECAP process and subsequently substituted by a new one according to which the basal planes were oriented close to the shear plane in ECAP (E3 and E5 samples). ECAP processed samples with such orientations thus feature much lower asymmetry in mechanical behavior and can exhibit excellent ductility at room temperature (Agnew et al., 2004; Al-Maharbi et al., 2011; Kim et al., 2003).

Figs. 8 and 9 display a collection of tensile and compression curves referred to the different alloy conditions investigated. It is observed that, starting from the as received condition (A sample) up to sample E2, by increasing the number of passes, UTS as well as TYS decrease form 339
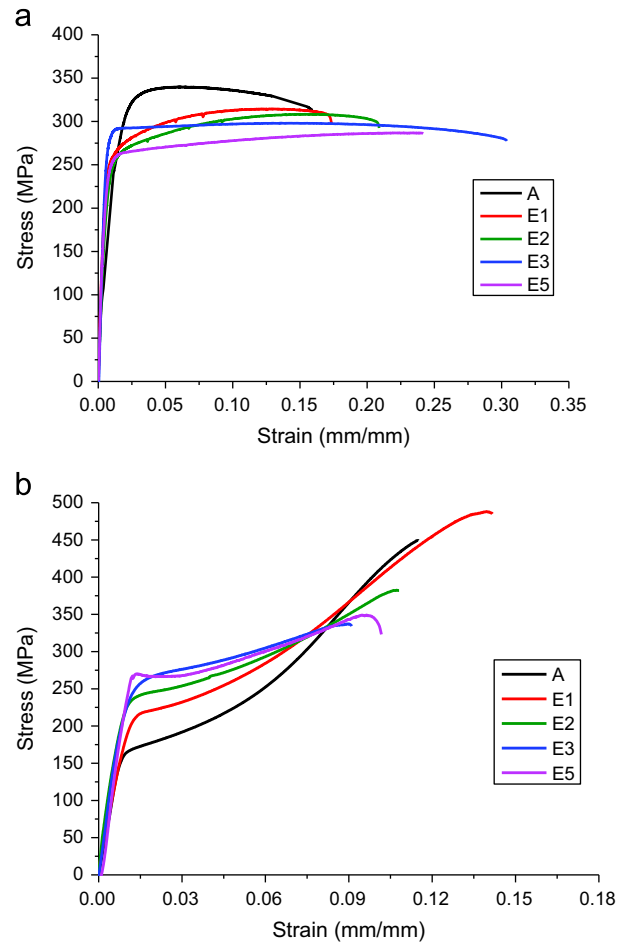

Fig. 8 – Tensile (a) and compressive (b) stress–strain curves measured at room temperature of the as-received and the ECAP processed ZK60 alloy.
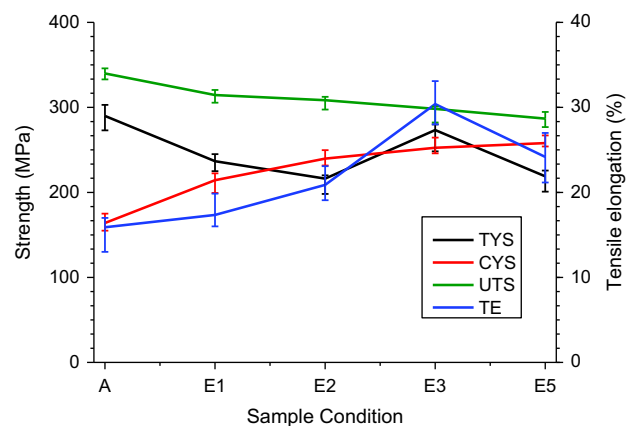

Fig. 9 – Tensile and compression properties of ZK60 alloy as a function of samples condition. UTS: tensile strength; TYS: tensile yield strength; TE: tensile elongation; CYS: compression yield strength.

and 290 MPa to 308 and 216 MPa, respectively, even though from Figs. 2 and 3a, a clear grain refinement effect was evident. A decrease of resultant TYS and UTS values are

mainly attributed to the weakening of the initial fiber texture (Fig. 5a and b) by increasing the texture intensity and the Schmid factor from 5.7 and 0.17 to 9.2 and 0.24, respectively. Accordingly, the texture modification played a dominant role in the first two steps and it compensates for grain refining strengthening effect, leading to a decrease in both TYS and UTS. Further ECAP passes (E3) gave rise to a significant TYS improvement, up to 273 MPa, that was also accompanied by higher fracture ductility (TE of about 30%). In other words, the texture softening effect is stronger than the strengthening effect given by grain refining by ECAP. Meaningful ameliora-tion in both strength and fracture elongation obtained in E3 sample can be explained by two distinct observations. First, as stated, a uniform and equiaxed ultra-fine grained micro-structure with grain size of 0.6 μm was achieved in E3 sample (Fig. 3b). Hence, due to the grain boundary strengthening, the TYS alloy was much higher than that of the previous condi-tion (E2) according to the Hall–Petch relationship. Further-more, formation of a newly introduced shear texture (Fig. 5c) with a higher maximum texture intensity accompanied by activation of non-basal slip systems due to grain boundary compatibility stress (Koike et al., 2003) as well as grain boundary sliding (GBS) at room temperature (Lu et al., 2014; Tan and Tan, 2003), both induced a significant improvement of TE of about 30%. In short, in the case of E3 sample, a combination of grain refinement and texture development is responsible for improved strength and ductility.

By increasing the number of passes at 150 °C (sample E5), all tensile features including TYS, UTS and TS dropped. Nevertheless, the UTS drop was not as remarkable as TYS and TE. As discussed before, for this condition the rotation of a high fraction of basal planes from 52° to 43° to the long-itudinal axis (Fig. 5c and d) formed a more dominant and stabilized texture. The modification in texture, beside increasing Schmid factor for (0 0 0 1) ⟨1 1 $\overline{2}$ 0⟩ basal slip from 0.30 to 0.35 (Figs. 5 and 6d), brings about an improved basal slip activity causing lowering stress required for yielding (softening effect) and thereby justifying the decrease in TYS from 273 to 219 MPa for sample E5. Moreover, an additional 4 passes at 150 °C led to grain growth (E5 sample) from about 0.6 μm to 1 μm (Fig. 3b and c), undermining the GBS effect

whereby higher ductility during tensile deformation could be obtained. These reasons are supposed to be responsible for the drop of TE values, from 30 to 24%.

In contrast to tensile behavior, ECAP process revealed to induce a marked compressive strengthening starting from the first pass, due to favorable combination of texture hard-ening and grain size strengthening, resulting in a rise of the CYS from 164 to 258 MPa (Fig. 8b and Fig. 9). Furthermore, since the tensile-compressive mechanical anisotropy is clo-sely related to generation of {1 0 $\overline{1}$ 2} ⟨1 0 $\overline{1}$ 1⟩ twins, the mechanical anisotropy was reduced by grain refinement and texture modification induced by ECAP (e.g. from A to E3) due to suppression of twin generation by activation of non-basal slipping systems.

3.3.3. Fractography

A view of tensile fractured samples A and E3 is displayed in Fig. 10. An almost horizontal fracture surface perpendicular to the tensile axis was detected in the sample A while a macroscopic shear fracture at about 45° to the mentioned axis was found in sample E3, implying that a great deal of the basal planes were coinciding with the shear plane in ECAP sample, which is consistent with observed texture (Fig. 5c). Thus, as it was discussed in the previous section, E3 sample exhibited a decent ductility at room temperature.
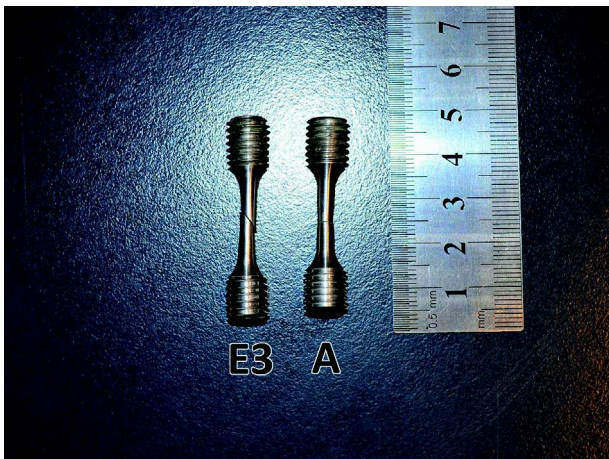

Fig. 10 – Macrographs of tensile fracture of (a) E3 and (b) A ZK60 alloys at room temperature.
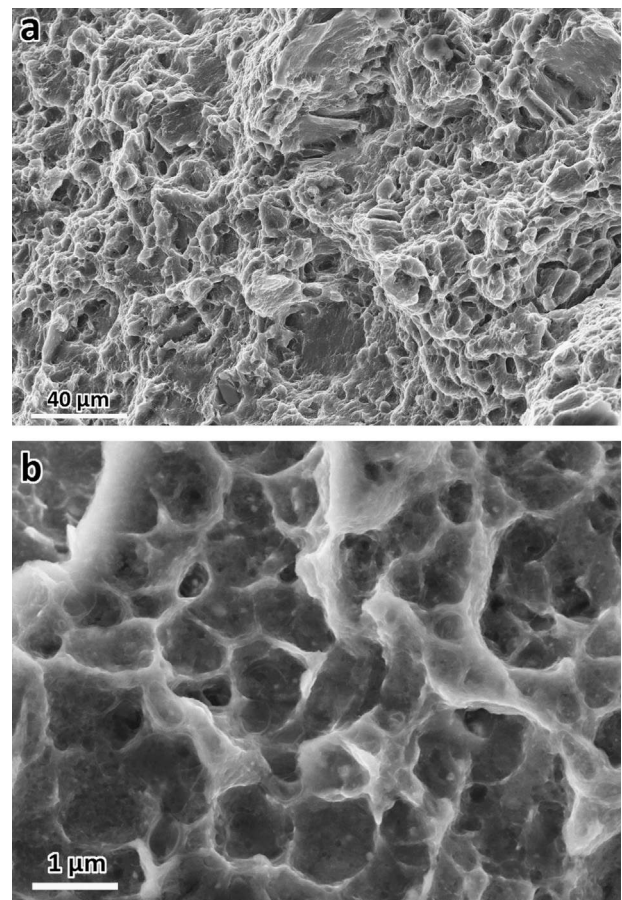

Fig. 11 – SEM views of the fracture surfaces of samples tensile broken samples: (a) A, (b) E3.

Fig. 11 reveals SEM fractographs of samples A and E3. It can be seen from Fig. 11a that a large number of dimples and cleavage planes are observed on the fracture surface, implying that sample A experienced a mixed fracture mode of ductile–brittle type. In contrast, Fig. 11b shows the E3 sample fracture surface with evidence of a much larger fraction of very fine and equiaxed dimples separated by sharp ridges, which are almost uniform in size, representing the typical features of markedly ductile fracture behavior.

3.4. Corrosion behavior

Fig. 12 shows the OCP plots of samples A and E3 for 18 h. It is observed that, within the first five hours of OCP, there is a mild shift toward nobler potentials, after which a steady state condition is set. Sample A shows a slightly nobler free corrosion potential (-1.49 V vs. Ag/AgCl) compared to sample E3 (-1.51 V vs. Ag/AgCl). This potential difference of 20 mV is
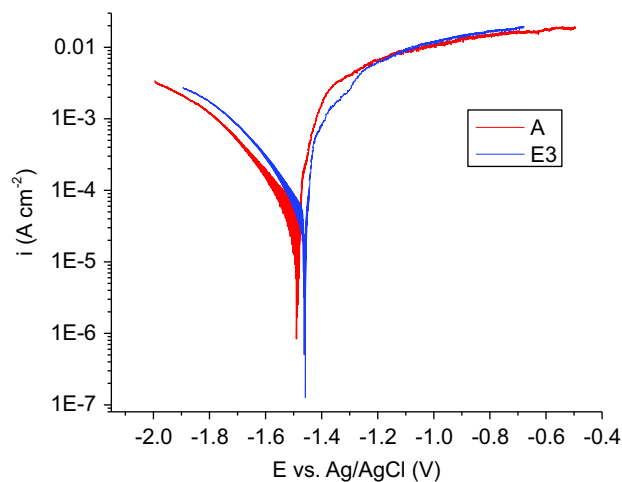
however supposed to be not enough significant to imply a nobler behavior of this sample.

Fig. 13 shows the the potentiodynamic measurements of A and E3 samples. A slight difference of about 20 mV in free corrosion potential is observed in potentiodynamic curves, implying again the comparable thermodynamic behavior of the as-received and ECAP processed samples. Based on the calculated Tafel extrapolation data of the polarization curves, both A and E3 samples show similar corrosion current densities of 60.4 and 56.2 μA/cm^2, respectively, revealing similar practical corrosion rates. Moreover, the anodic parts of the two curves are well overlapping confirming a comparable behavior in active and passive regions. Accordingly, from the electrochemical point of view, no obvious and definite superiority in corrosion behavior of one of the two investigated conditions for the ZK60 alloy can be inferred.

Fig. 14 shows the weight loss trend of samples A and E3 in PBS solution as a function of time, up to 96 h. A clear distinction in weight loss trend of the two samples is now observed with the as extruded sample A, featuring a higher weight loss rate than the ECAP processed E3 sample. These data are apparently inconsistent with the results obtained from electrochemical measurements suggesting a comparable behavior of the two conditions. Similar results have been already reported in the literature and priority has been given to the weight loss evaluation (Shi et al., 2010). The clue behind such priority could be found in the fundamental requirements of the Tafel extrapolation method that are absolutely likely to be violated in case of magnesium. In fact, the necessity of a single anodic or cathodic reaction for a reliable application of Tafel extrapolation is missing in case of magnesium. In the cathodic part of the polarization curve, hydrogen is evolved through separate reactions on the covered and uncovered areas by a protective film. The same applies to the magnesium dissolution in the anodic part of the polarization curve. Furthermore, particle undermining that is of significant importance in the corrosion of magnesium and its alloys, can hardly be included in any electrochemical method to measure the corrosion rate (Song and Atrens, 2003). For all these reasons, in this study the comparison in corrosion rate was justified mostly based on the
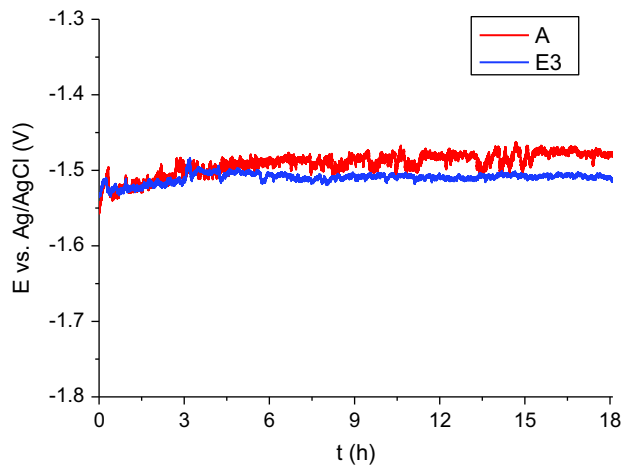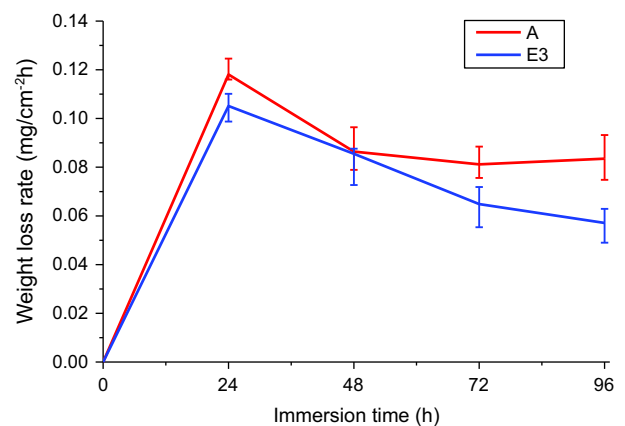

Fig. 12 – Evolution of corrosion potential of samples A and E3 with time in PBS at 37 °C.

Fig. 13 – Potentiodynamic polarization curves by immersion in PBS of ZK60 alloy before and after ECAP.

Fig. 14 – Corrosion rate curves of A and E3 samples as a function of time during immersion in PBS.
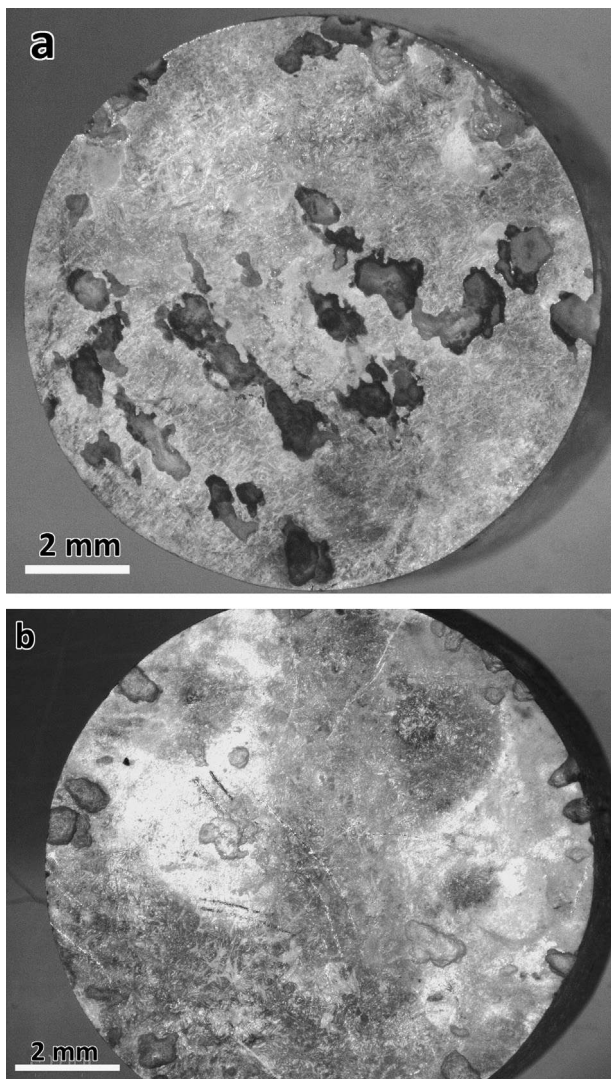
Fig. 15 – General view of the corrosion surfaces of the materials immersed in PBS for 96 h: (a) A sample, (b) E3 sample.

weight loss measurements and consequently, a higher corrosion rate of the as-received sample was ruled out.

In order to better understand the processes contributing in the final corrosion of material and build up a scheme of the corrosion mechanism, microstructural characterization of the corroded samples was carried out at different levels, namely, stereoscopic and SEM studies for macro and microstructure assessments, respectively.

Fig. 15 depicts the stereoscopic images of surface conditions of A and E3 samples after 96 h immersion in PBS solution and following the removal of corrosion products by chromic acid. In sample A, the formation of large holes as a consequence of pit development is observed, thus confirming the advanced level of localized corrosion occurrence. Since in the as-received sample intermetallic particles were observed to be larger and more heterogeneously dispersed in the matrix (see Fig. 2), it is believed that the micro-galvanic effect could be more pronounced, promoting severe corrosion conditions around rather coarse

second-phase particles (Atrens et al., 2011; Song and Atrens, 1999; Zeng et al., 2011). In E type samples, due to strong ECAP induced deformation, second phase particles are refined to a higher extent and are more homogeneously distributed in the matrix. Accordingly, localized corrosion is limited to smaller areas and degradation is observed mainly by a uniform corrosion regime.

The assessment of these general observations was supported by SEM studies carried out on the two samples. For this purpose, samples A and E were immersed in the PBS solution and in order to look at the starting stages of the corrosion, immersion was stopped after short periods of 4 and 8 h. This was mainly aimed to avoid advanced levels of degradation just in order to be able to focus on the initiation of corrosion where any probable localization of the corrosion around second phase particles could be monitored. Fig. 16 shows the SEM micrographs of sample A after 4 and 8 h immersion in PBS and subsequent 5 min washing in chromic acid. As seen, different regions with different levels of corrosion advance can be distinguished in low magnification images (Fig. 16a) namely, large holes (elongated dark areas) and bright root-like corroded areas. Formation of large holes in the range of several hundred micrometers (as magnified in Fig. 16b) suggests that even in short exposure times to the corrosive environment, serious damage can happen. Magnified view of root-like regions (Fig. 16c and d in two magnifications) reveals a sort of filiform corrosion (filamentary corrosion occurring on metal surfaces) that is actually the dominant mode here in terms of covered surface area. Since this type of corrosion basically occurs under the protective films (the reason for which, this type of corrosion is also called *underfilm corrosion*) (Fontana, 1985), either an externally applied protective film such as enamel or lacquer coatings or intrinsically formed films such as passive oxide films, attribution of such phenomenon to magnesium is quite plausible (Slabaugh and Grotheer, 1954).

Although there are few reports of filiform corrosion on magnesium in general context in the literature (Williams and Grace, 2011), considering the intrinsic susceptibility of magnesium to the passive film formation (Song and Atrens, 1999), it is interesting that such kind of corrosion has rarely, if not saying never, been reported in the context of magnesium based biodegradable applications.

Noting the superficial nature of filiform attack that does not deeply destroy the metallic components but mainly affects the surface and appearance (Fontana, 1985), this corrosion type cannot be considered as the origin of large holes. Instead, looking at more prolonged stages of corrosion, one can infer that the filaments widen as well by time, and finally meet each other laterally forming a flat surface (see Fig. 16e for sample A after 8 h immersion). Therefore, this process contributes effectively in the general corrosion of magnesium. Obviously, while forming, these filaments are covered by corrosion products, namely, $Mg(OH)_2$. In current micrographs however, the corrosion products have been removed by chromic acid and thus, the corrosion sub-layer can be observed as seen in Fig. 16f. It is seen that due to the corrosion attack, grains are appearing in these regions with interesting signs of preferential crystallographic direction of corrosion advance in individual grains.
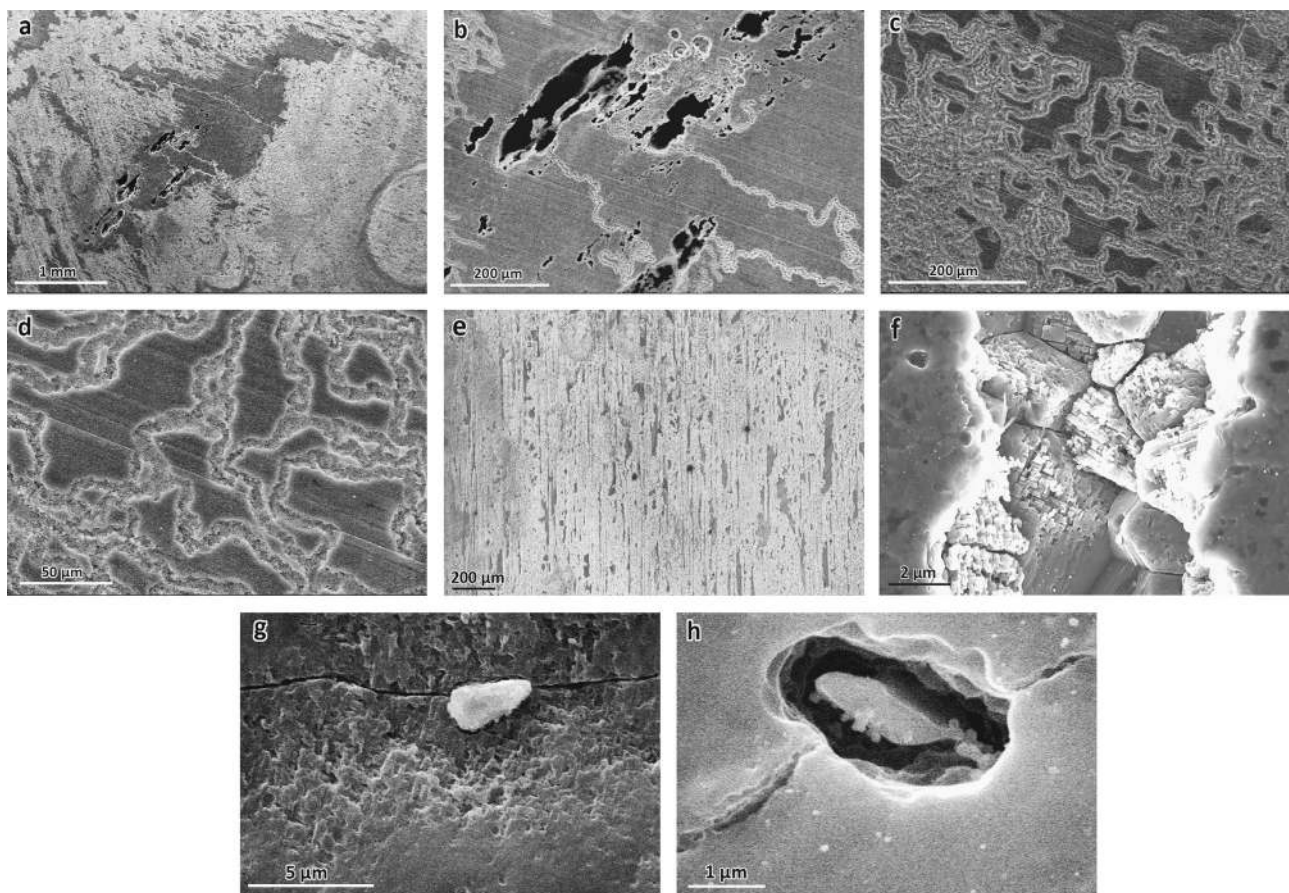
Fig. 16 – SEM micrographs of sample A immersed in PBS; (a) general view of the corroded surface after 4 h, (b) large localized holes formed within 4 h, (c) and (d) root-like filiform corrosion in two magnifications, (e) lateral coalescence of filaments after 8 h immersion in PBS, contributing to general corrosion, (f) sub-layer of corroded filaments showing Mg grains and preferential corrosion direction in individual grains and (g) and (h) two examples of localized corrosion around second phase particles.

To better investigate on this effect, the analysis was then focused on the regions around the large holes in the search for evidences of the primary stages of the hole formation. Interestingly, it was observed that whenever a second phase particle with a size exceeding 1μm was found on the surface, a localized corrosion around the particle was visible, accelerating the magnesium matrix dissolution. Two examples of such phenomenon are given in Fig. 16g and h. Accordingly, it can be supposed that the large holes are formed in the regions where a primary accumulation of second phase particles existed in the as-received material. Considering the point that the as-received samples are produced through an extrusion process (the usual industrial method of producing wrought Mg alloy bars), it becomes more comprehensible the idea of accumulation of the second phase particles in some certain lines along the extrusion direction. These regions are those in which the large elongated holes will form (Fig. 16b) due to accelerated dissolution of magnesium surrounding the second phase particles.

To ascertain the nature of these particles, EDS analysis was performed on them, as shown Fig. 17. In Fig. 17a an overview of the location of the particle to be analyzed is depicted. The region encircled by dashes represents a similar feature to those encircled in Fig. 2, and hence, supposedly, an accumulation

line of second phased particles along the extrusion direction. In magnified view of Fig. 17b, it is seen that presence of large holes around this line is apparent (black arrows). A small particle is shown nearby a corrosion filament (pointed to by a white arrow), that is further analyzed by an EDS line scan as shown in Fig. 17c and d. The line starts at A and ends at E, the particle being located at point D. Interestingly, exactly at point D (the particle), Mg signal decreases remarkably and instead, those of Zn and Zr increase. This can be understood as a clear confirmation of the presence of a secondary phase of Zn–Zr elements. Mg signal decreases also in the valley of the filament. However, no intensified Zn or Zr signals is observed there. Thus, it is just related to Mg dissolution and of course, some topographic effects attenuating the signal received from the valley. Oxygen signal increases at both valley and particle locations, indicating some residues of corrosion products not removed completely by chromic acid. According to all these observations, the second phase nature of the bright particles and their contribution in the localized corrosion and in turn, formation of large holes where their accumulation happens, is concluded.

In order to assess the role of ECAP on the corrosion behavior and the probable differences it could make, SEM studies on the corroded sample E after 4 and 8 h immersion in
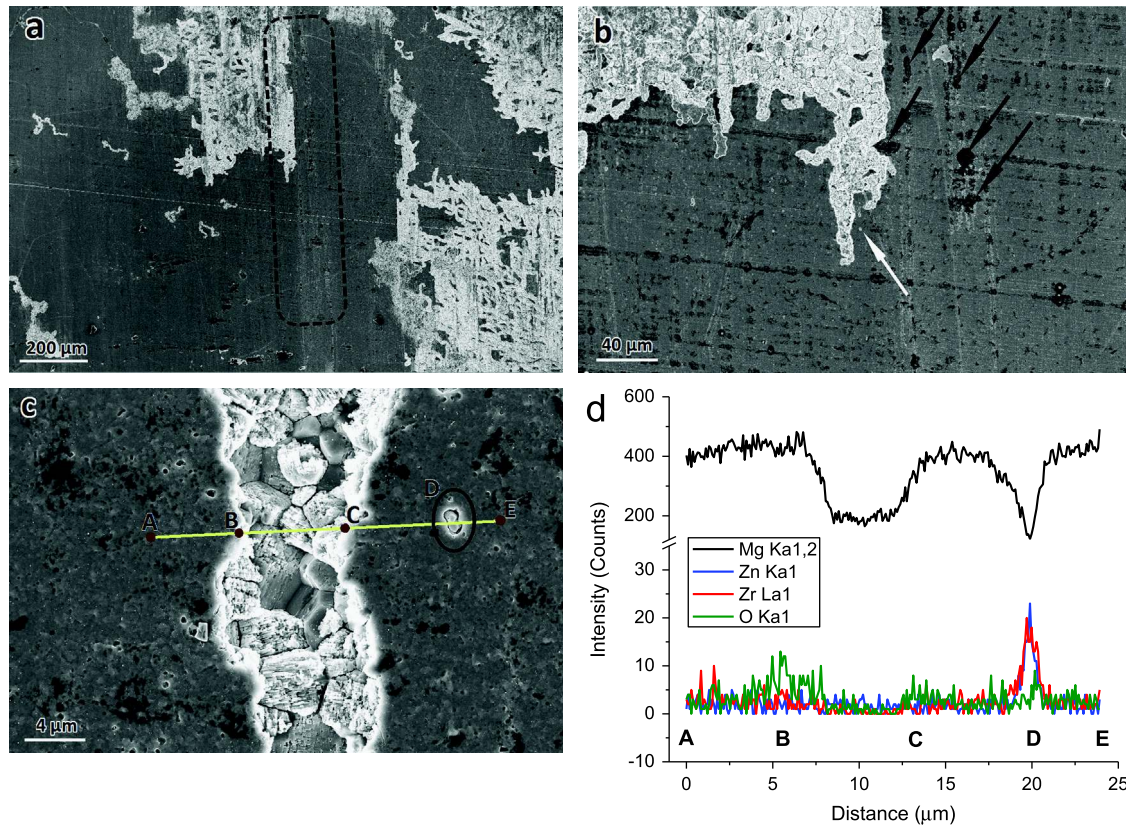
Fig. 17 – SEM micrographs of sample A immersed in PBS; (a) encircled a region of accumulation of second phase particles around the extrusion line, (b) magnified view of a, showing a population of pits around the extrusion line (black arrows) and second a relatively large second phase particle (white arrow), (c) magnified view of b, showing localized corrosion around the particle nearby a corrosion filament and (d) EDS line scan analysis of the path shown in c.
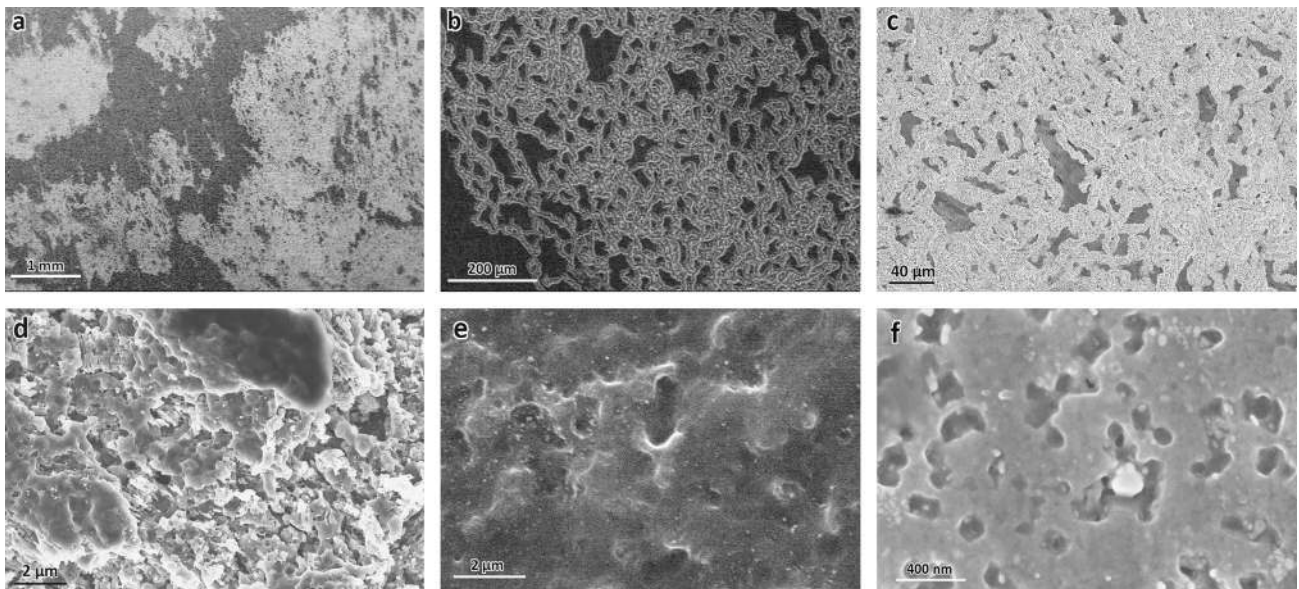

Fig. 18 – SEM micrographs of sample E3 immersed in PBS; (a) general view of the corroded surface after 4 h, (b) root-like filiform corrosion, (c) lateral coalescence of filaments after 8 h immersion in PBS, contributing to general corrosion, (d) sub-layer of corroded filaments (e) and (f) two examples of refined and well dispersed second phase particles.

PBS were conducted, as shown in Fig. 18. The general outlook of this sample is similar to sample A, showing the same root-like features spreading over the surface (Fig. 18a and b).

However, the population of large holes is negligible compared to sample A. Lateral widening of the filaments in longer immersion times (8 h) and their coalescence is observed also
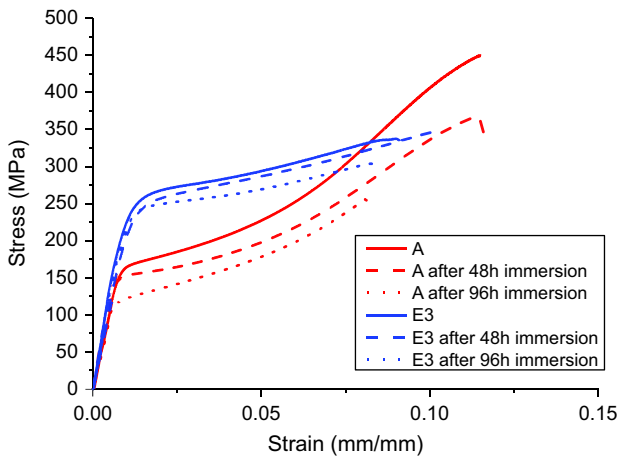
Fig. 19 – Compressive stress–strain curves of the samples A and E3 at room temperature before and after immersion in PBS.

in this sample (Fig. 18c). However, in the corrosion sub-layer, morphology of the grains is not easily recognizable (Fig. 18d), probably, due to smaller grain size and evolved texture of the ECAP-processed sample. The other noticeable difference between this sample and sample A was the absence of second phase particles larger than 200 nm. As shown in Fig. 18e and f, all second phase particles in sample E are broken to very fine sizes (around 100 nm) during the ECAP process and dispersed homogeneously in the matrix, minimizing the risk of localized corrosion.

To evaluate the effect of corrosion on mechanical properties of ECAP and non-ECAP processed alloys compression test on samples immersed at different times was carried out. Fig. 19 compares the compressive behavior of samples A and E3 before and after immersion for 48 and 96 h. These data are of paramount importance for the evaluation of residual strength of devices after partial biodegradation. It is confirmed that, for both A and E3 samples, the compressive strength decreases with increasing immersion time. In particular, it can be stated that after 96 h of immersion the CYS of sample A decreases by 28%, from 164 to 119 MPa. However, the reduction in compressive strength for sample E3 even after 96 h of immersion was 12%, from 252 to 220 MPa. This confirms that for UFG sample the corrosion behavior is such that mechanical degradation progresses at a slower rate than in the as extruded samples.

4. Conclusion

ECAP was carried out on ZK60 Mg alloy aimed at producing ultra-fine grained structure and to acquire a better understanding of the effect of UFG structure on mechanical and corrosion properties for potential applications in biodegradable devices. The conclusions can be summarized as follows:

1. ECAP is an effective grain-refinement technique for ZK60 Mg alloy. A strategy consisting in three-step processing at decreasing temperatures was developed. Accordingly, the coarse grained and segregation banded microstructure of the as-extruded samples was substituted by a homogeneous equiaxed-grain structure with average size of about 600 nm. After several ECAP passes (i.e. four passes for the investigated temperatures), saturation of properties was achieved so that additional passes could not further refine the microstructure.

2. A detailed texture investigation determined the texture evolution during ECAP processing. The initial fiber texture of ZK60 extruded alloy was progressively disintegrated during first two ECAP steps. Afterwards, at the final step of the process (150 °C) the fiber was fully replaced by a newly stronger texture component featuring basal planes preferentially aligned along ECAP shear plane, with higher maximum texture intensity and Schmid factor values.

3. Microstructural, texture, fracture surface and mechanical analyses revealed that a combination of grain refinement and texture development led to an improvement of both strength and ductility in E3, which refers to 4 ECAP passes at any corresponding temperature, condition. That is, elongation to failure of about 100% was obtained in E3 sample while keeping relatively high yield and ultimate tensile strength.

4. Mechanical anisotropy was appreciably reduced by grain refinement induced by ECAP in sample E3 due to activation of non-basal slip systems at the UFG scale. When ECAP passes exceeded a given threshold (E3), the tensile mechanical features started decreasing, which was attributed to the texture modification as well as increasing Schmid factor for basal slip. Moreover, texture development accompanied by grain refinement led to progressively increase in CYS as ECAP process advances.

5. Corrosion studies showed that the electrochemical behavior, namely the free corrosion potential, is not significantly affected by the ECAP-induced microstructural refinement. However, corrosion rate monitoring by weight loss revealed a clear improvement of corrosion resistance in UFG alloys compared to extruded materials. Morphological studies of corroded surfaces demonstrated that a filiform-like corrosion attack was responsible for the initiating stage. This corrosion mode remained restrained to surface and lateral widening of the filaments, while the coalescence of the pits contributed to general corrosion. On the other hand, remarkable pitting and localized corrosion was observed mainly in the as-received sample around the accumulation areas of the relatively large second-phase particles. In ECAP processed alloys in contrast, a shift of corrosion regime from localized pitting to a more uniform corrosion mode was observed mainly due to the second phase refinement and redistribution.

6. The reduction in CYS for E3 and A samples after 96 h immersion in the PBS were 12% and 28% respectively. That is, the rate of loss of mechanical integrity in the UFG samples was lower than that in the as-received sample.

Acknowledgements

REFERENCES

Agnew, S.R., Horton, J.A., Lillo, T.M., Brown, D.W., 2004. Enhanced ductility in strongly textured magnesium produced by equal channel angular processing. Scr. Mater. 50, 377–381, http://dx.doi.org/10.1016/j.scriptamat.2003.10.006.

Al-Maharbi, M., Karaman, I., Beyerlein, I.J., Foley, D., Hartwig, K.T., Kecskes, L.J., Mathaudhu, S.N., 2011. Microstructure, crystallographic texture, and plastic anisotropy evolution in an Mg alloy during equal channel angular extrusion processing. Mater. Sci. Eng., A 528, 7616–7627, http://dx.doi.org/10.1016/j.msea.2011.06.043.

Alvarez-Lopez, M., Pereda, M.D., del Valle, J.A., Fernandez-Lorenzo, M., Garcia-Alonso, M.C., Ruano, O.A., Escudero, M.L., 2010. Corrosion behaviour of AZ31 magnesium alloy with different grain sizes in simulated biological fluids. Acta Biomater. 6, 1763–1771, http://dx.doi.org/10.1016/j.actbio.2009.04.041.

Argade, G.R., Panigrahi, S.K., Mishra, R.S., 2012. Effects of grain size on the corrosion resistance of wrought magnesium alloys containing neodymium. Corros. Sci. 58, 145–151, http://dx.doi.org/10.1016/j.corsci.2012.01.021.

ASTM-G102-89, 1989. Standard Practice for Calculation of Corrosion Rates and Related Information from Electrochemical Measurements. CERN Doc. Serv.

Atrens, A., Liu, M., Zainal Abidin, N.I., 2011. Corrosion mechanism applicable to biodegradable magnesium implants. Mater. Sci. Eng., B 176, 1609–1636, http://dx.doi.org/10.1016/j.mseb.2010.12.017.

Bohlen, J., Nürnberg, M.R., Senn, J.W., Letzig, D., Agnew, S.R., 2007. The texture and anisotropy of magnesium–zinc–rare earth alloy sheets. Acta Mater. 55, 2101–2112, http://dx.doi.org/10.1016/j.actamat.2006.11.013.

Chino, Y., Kimura, K., Hakamada, M., Mabuchi, M., 2008. Mechanical anisotropy due to twinning in an extruded AZ31 Mg alloy. Mater. Sci. Eng., A 485, 311–317, http://dx.doi.org/10.1016/j.msea.2007.07.076.

Del Valle, J.A., Carreño, F., Ruano, O.A., 2006. Influence of texture and grain size on work hardening and ductility in magnesium-based alloys processed by ECAP and rolling. Acta Mater. 54, 4247–4259, http://dx.doi.org/10.1016/j.actamat.2006.05.018.

Dumitru, F.-D., Higuera-Cobos, O.F., Cabrera, J.M., 2014. ZK60 alloy processed by ECAP: Microstructural, physical and mechanical characterization. Mater. Sci. Eng., A 594, 32–39, http://dx.doi.org/10.1016/j.msea.2013.11.050.

Emley, Edward F., 1966. Principles of Magnesium Technology, first ed. Pergamon Press.

Fontana, M.G., 1985. Corrosion Engineering, third ed. McGraw-Hill Book Company, New York.

Gao, J.H., Guan, S.K., Ren, Z.W., Sun, Y.F., Zhu, S.J., Wang, B., 2011. Homogeneous corrosion of high pressure torsion treated Mg–Zn–Ca alloy in simulated body fluid. Mater. Lett. 65, 691–693, http://dx.doi.org/10.1016/j.matlet.2010.11.015.

Ge, Q., Dellasega, D., Demir, A.G., Vedani, M., 2013. The processing of ultrafine-grained Mg tubes for biodegradable stents. Acta Biomater. 9, 8604–8610, http://dx.doi.org/10.1016/j.actbio.2013.01.010.

Gholinia, A., Prangnell, P.B., Markushev, M.V., 2000. The effect of strain path on the development of deformation structures in severely deformed aluminium alloys processed by ECAE. Acta Mater. 48, 1115–1130, http://dx.doi.org/10.1016/S1359-6454(99)00388-2.

Goodman, S.B., Davidson, J.A., Fornasier, V.L., Mishra, A.K., 1993. Histological response to cylinders of a low modulus titanium alloy (Ti–13Nb–13Zr) and a wear resistant zirconium alloy (Zr–2.5Nb) implanted in the rabbit tibia. J. Appl. Biomater. 4, 331–339, http://dx.doi.org/10.1002/jab.770040407.

Gu, X., Zheng, Y., Cheng, Y., Zhong, S., Xi, T., 2009. In vitro corrosion and biocompatibility of binary magnesium alloys. Biomaterials 30, 484–498, http://dx.doi.org/10.1016/j.biomaterials.2008.10.021.

Gu, X.-N., Zheng, Y.-F., 2010. A review on magnesium alloys as biodegradable materials. Front. Mater. Sci. Chin. 4, 111–115, http://dx.doi.org/10.1007/s11706-010-0024-1.

Gunde, P., Hänzi, A.C., Sologubenko, A.S., Uggowitzer, P.J., 2011. High-strength magnesium alloys for degradable implant applications. Mater. Sci. Eng., A 528, 1047–1054, http://dx.doi.org/10.1016/j.msea.2010.09.068.

He, Y., Pan, Q., Qin, Y., Liu, X., Li, W., Chiu, Y., Chen, J.J.J., 2010. Microstructure and mechanical properties of ZK60 alloy processed by two-step equal channel angular pressing. J. Alloys Compd. 492, 605–610, http://dx.doi.org/10.1016/j.jallcom.2009.11.192.

Hermawan, H., Dubé, D., Mantovani, D., 2010. Developments in metallic biodegradable stents. Acta Biomater. 6, 1693–1697, http://dx.doi.org/10.1016/j.actbio.2009.10.006.

Hutchinson, W.B., Barnett, M.R., 2010. Effective values of critical resolved shear stress for slip in polycrystalline magnesium and other hcp metals. Scr. Mater. 63, 737–740, http://dx.doi.org/10.1016/j.scriptamat.2010.05.047 (Viewpoint set no. 47 Magnesium Alloy Science and Technology).

Iwahashi, Y., Wang, J., Horita, Z., Nemoto, M., Langdon, T.G., 1996. Principle of equal-channel angular pressing for the processing of ultra-fine grained materials. Scr. Mater. 35, 143–146, http://dx.doi.org/10.1016/1359-6462(96)00107-8.

Kim, W.J., An, C.W., Kim, Y.S., Hong, S.I., 2002. Mechanical properties and microstructures of an AZ61 Mg Alloy produced by equal channel angular pressing. Scr. Mater. 47, 39–44, http://dx.doi.org/10.1016/S1359-6462(02)00094-5.

Kim, W.J., Hong, S.I., Kim, Y.S., Min, S.H., Jeong, H.T., Lee, J.D., 2003. Texture development and its effect on mechanical properties of an AZ61 Mg alloy fabricated by equal channel angular pressing. Acta Mater. 51, 3293–3307, http://dx.doi.org/10.1016/S1359-6454(03)00161-7.

Koike, J., Kobayashi, T., Mukai, T., Watanabe, H., Suzuki, M., Maruyama, K., Higashi, K., 2003. The activity of non-basal slip systems and dynamic recovery at room temperature in fine-grained AZ31B magnesium alloys. Acta Mater. 51, 2055–2065, http://dx.doi.org/10.1016/S1359-6454(03)00005-3.

Lu, F.M., Ma, A.B., Jiang, J.H., Yang, D.H., Yuan, Y.C., Zhang, L.Y., 2014. Formation of profuse long period stacking ordered microcells in Mg–Gd–Zn–Zr alloy during multipass ECAP process. J. Alloys Compd. 601, 140–145, http://dx.doi.org/10.1016/j.jallcom.2014.02.175.

Máthis, K., Nyilas, K., Axt, A., Dragomir-Cernatescu, I., Ungár, T., Lukáč, P., 2004. The evolution of non-basal dislocations as a function of deformation temperature in pure magnesium determined by X-ray diffraction. Acta Mater. 52, 2889–2894, http://dx.doi.org/10.1016/j.actamat.2004.02.034.

Miao, Q., Hu, L., Wang, X., Wang, E., 2010. Grain growth kinetics of a fine-grained AZ31 magnesium alloy produced by hot rolling. J. Alloys Compd. 493, 87–90, http://dx.doi.org/10.1016/j.jallcom.2009.12.049.

Mostaed, E., Ge, Q., Vedani, M., De Oliveira, Botelho, Zanella, P.A., Deflorian, C., F., 2013. Investigation on the influence of grain size on strength, ductility, and corrosion properties in Mg and Mg–Zn based alloys for biodegradable stents. Eur. Cell. Mater. 26, 84.

Obara, T., Yoshinga, H., Morozumi, S., 1973. {1122} $\langle \bar{1}\,\bar{1}23\rangle$ Slip system in magnesium. Acta Metall. 21, 845–853, http://dx.doi.org/10.1016/0001-6160(73)90141-7.

Pérez-Prado, M.T., Ruano, O.A., 2002. Texture evolution during annealing of magnesium AZ31 alloy. Scr. Mater. 46, 149–155, http://dx.doi.org/10.1016/S1359-6462(01)01212-X.

Robson, J.D., Henry, D.T., Davis, B., 2009. Particle effects on recrystallization in magnesium–manganese alloys: particle-

stimulated nucleation. Acta Mater. 57, 2739–2747, http://dx.doi.org/10.1016/j.actamat.2009.02.032.

Saris, N.-E.L., Mervaala, E., Karppanen, H., Khawaja, J.A., Lewenstam, A., 2000. Magnesium: an update on physiological, clinical and analytical aspects. Clin. Chim. Acta 294, 1–26, http://dx.doi.org/10.1016/S0009-8981(99)00258-2.

Segal, V.M., 1999. Equal channel angular extrusion: from macromechanics to structure formation. Mater. Sci. Eng., A 271, 322–333, http://dx.doi.org/10.1016/S0921-5093(99)00248-8.

Shi, Z., Liu, M., Atrens, A., 2010. Measurement of the corrosion rate of magnesium alloys using Tafel extrapolation. Corros. Sci. 52, 579–588, http://dx.doi.org/10.1016/j.corsci.2009.10.016.

Slabaugh, W., Grotheer, M., 1954. Mechanism of filiform corrosion. Ind. Eng. Chem. 46, 1014–1016.

Song, G., 2007. Control of biodegradation of biocompatable magnesium alloys. Corros. Sci. 49, 1696–1701, http://dx.doi.org/10.1016/j.corsci.2007.01.001.

Song, G., Atrens, A., 2003. Understanding magnesium corrosion—a framework for improved alloy performance. Adv. Eng. Mater. 5, 837–858, http://dx.doi.org/10.1002/adem.200310405.

Song, G.L., Atrens, A., 1999. Corrosion mechanisms of magnesium alloys. Adv. Eng. Mater. 1, 11–33, http://dx.doi.org/10.1002/(SICI)1527-2648(199909)1:1<11::AID-ADEM11>3.0.CO;2-N.

Tan, J.C., Tan, M.J., 2003. Dynamic continuous recrystallization characteristics in two stage deformation of Mg–3Al–1Zn alloy sheet. Mater. Sci. Eng., A 339, 124–132, http://dx.doi.org/10.1016/S0921-5093(02)00096-5.

Tang, W.N., Chen, R.S., Zhou, J., Han, E.H., 2009. Effects of ECAE temperature and billet orientation on the microstructure, texture evolution and mechanical properties of a Mg–Zn–Y–Zr alloy. In: Fifth International Conference on Physical and Numerical Simulations of Material Processing (ICPNS 2007) held at Zhengzhou, China, October 23–27, 2007. Mater. Sci. Eng., A 499, 404–410. http://dx.doi.org/10.1016/j.msea.2008.09.048.

Wang, Y., Guan, S., Zeng, X., Ding, W., 2006. Effects of RE on the microstructure and mechanical properties of Mg–8Zn–4Al magnesium alloy. Mater. Sci. Eng., A 416, 109–118, http://dx.doi.org/10.1016/j.msea.2005.09.104.

Wang, Y.N., Huang, J.C., 2007. The role of twinning and untwinning in yielding behavior in hot-extruded Mg–Al–Zn alloy. Acta Mater. 55, 897–905, http://dx.doi.org/10.1016/j.actamat.2006.09.010.

Williams, G., Grace, R., 2011. Chloride-induced filiform corrosion of organic-coated magnesium. Electrochim. Acta 56, 1894–1903, http://dx.doi.org/10.1016/j.electacta.2010.09.005 (ADVANCES IN CORROSION SCIENCE FOR LIFETIME PREDICTION AND SUSTAINABILITYSelection of papers from the 8th ISE Spring Meeting2-5 May 2010, Columbus, OH, USA).

Witte, F., Hort, N., Vogt, C., Cohen, S., Kainer, K.U., Willumeit, R., Feyerabend, F., 2008. Degradable biomaterials based on magnesium corrosion. Curr. Opin. Solid State Mater. Sci. 12, 63–72, http://dx.doi.org/10.1016/j.cossms.2009.04.001.

Yamashita, A., Horita, Z., Langdon, T.G., 2001. Improving the mechanical properties of magnesium and a magnesium alloy through severe plastic deformation. Mater. Sci. Eng., A 300, 142–147, http://dx.doi.org/10.1016/S0921-5093(00)01660-9.

Zeng, R., Dietzel, W., Witte, F., Hort, N., Blawert, C., 2008. Progress and challenge for magnesium alloys as biomaterials. Adv. Eng. Mater. 10, B3–B14, http://dx.doi.org/10.1002/adem.200800035.

Zeng, R., Kainer, K.U., Blawert, C., Dietzel, W., 2011. Corrosion of an extruded magnesium alloy ZK60 component—the role of microstructural features. J. Alloys Compd. 509, 4462–4469, http://dx.doi.org/10.1016/j.jallcom.2011.01.116.